Keiser, A., Baumli, P., Vollmer, D., & Quéré, D. (2020). Universality of friction laws on liquid-infused materials. Physical Review Fluids, 5(1): 014005. doi:10.1103/PhysRevFluids.5.014005.

Online abstract:
https://journals.aps.org/prfluids/abstract/10.1103/PhysRevFluids.5.014005

Universality of friction laws on liquid-infused materials

Keiser, A., Baumli, P., Vollmer, D., & Quéré, D

Universality of the friction laws on liquid-infused materials

Armelle Keiser[1], Philipp Baumli[2], Doris Vollmer[2] & David Quéré[1]

[1] *Physique et Mécanique des Milieux Hétérogènes, UMR 7636 du CNRS, PSL Research University, ESPCI, 75005 Paris, France.*
[2] *Max Planck Institute for Polymer Research, Mainz, Germany*.

Armelle Keiser and Philipp Baumli equally contributed to this work.

Lubricant-infused surfaces (LIS) make drops remarkably mobile. However, the dynamics of those drops proved to be subtle, due to the numerous phases at stake (lubricant, drop, solid texture, air). In this article, we highlight the role played by a feature specific to LIS, namely the "foot" of oil surrounding the drops and drawn by their surface tension. Consequently, viscous dissipation can be localized in four distinct regions, which we tune independently through various experimental set-ups. Despite this complexity, we evidence a universal scaling for the friction law and reconciliate recent results produced on this topic.

Keywords: Liquid-infused surfaces, textured surfaces, friction, viscous dissipation.

Introduction

The so-called "liquid-infused surfaces" (LIS) recently attracted a lot of attention, due to the extremely low adhesion of water or aqueous solutions to them. These materials are covered by a microscopic texture in which oil is infused so that another liquid deposited on them faces an impregnated porous-like substrate on which it hardly pins [1-4]. Hence the liquid (hereafter generically called water) is highly mobile, yet with some friction [4-10] whose nature is still under debate, owing to the complexity of the situation [4, 6-9].

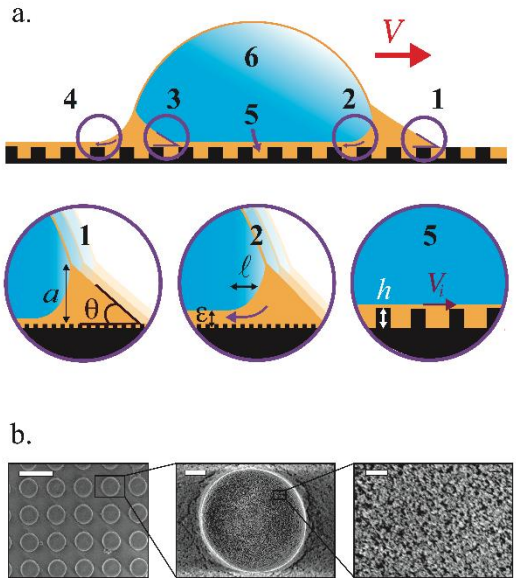

FIG1: a. Schematic of a drop moving at a speed *V* on a liquid-infused material. Water (or aqueous phase) is blue, while the lubricating oil is orange. Six main dynamical regions can be defined. Four of them concern the oil foot around the drop, with advancing (regions 1 and 3) and receding (regions 2 and 4) sides. The two other regions are the drop itself (region 6) and the oil film with thickness *h* within the texture (region 5). The oil foot (size *a*) is supposed asymmetric, with an advancing angle θ at the front (region 1) and a film of thickness ε at the rear (region 2). V_i (close up in region 5) is the water/oil interface velocity. **b.** SEM images of the texture made of NOA (Norland Optical Adhesive) on a glass slide and treated with colloidal particles (courtesy of Florian Geyer, MPIP). Left: top view of the pillar network (scale bar: 40 µm). Middle: close-up on one pillar (scale bar: 4 µm). Right: close-up on the nano-roughness at the pillar top (scale bar 400 nm).

We focus here on the generic case of a drop facing a liquid of higher viscosity, which corresponds to water on most non-volatile oils. Smith *et al.* [4] showed that friction then occurs in the oil meniscus (or foot) surrounding the drop and sketched in Fig. 1a. If this friction were that in the bulk of the foot (assumed to have a constant shape), it would have a classical Stokes nature, evidenced by a linear relationship between friction and speed. However, Daniel *et al.* [7] and Keiser *et al.* [6] suggested that the shape of the meniscus is speed dependent, leading to a non-linear relationship between friction and speed. It is worth discussing the generality of these ideas. A natural parameter, for instance, is the height of the underlying texture, and Daniel *et al.* argued that the scaling between the friction and speed might depend on this height, with a linear relationship for tall pillars and a non-linear one for short ones [7]. This change was attributed to the possibility of generating Landau-Levich oil films above short pillars, as drops move, while such films are absorbed by a tall texture [11-12]. We provide here new experiments in a broad range of velocity, allowing us to discuss the role of the menisci front in the dissipation process – with the aim of establishing the scaling form(s) of the friction.

Our main conclusion is that the scaling law for the friction is surprisingly universal, varying as the power 2/3 of speed on both short and tall pillars. However, the prefactor in the law does depend on the pillar height, a consequence of the existence or absence of Landau-Levich films

beneath the moving drop. A transition regime thus exists, depending on the pillar height and/or drop speed, where the scaling law is transiently lost. We finally confirm the generality of our results by studying two supplementary configurations, that of a drop confined in a Hele-Shaw cell, and that of a bubble rising along an inclined LIS plunged in a water bath.

Mobility of drops on LIS

We consider micro-pillars (with density ϕ = 23-25%) etched in SU8-resin after photolithography, then coated with nanometric colloids (Glaco Mirror Coat, Soft 99). This double scale of roughness is visible in Fig. 1b and it provides an ultra-low hysteresis once oil is infused [6, 13] and details on the preparation of the samples are given in the appendix. The lubricant is a silicone oil with surface tension γ_o = 20 mN/m and viscosity η_o =100 mPa·s while the drop is made of a water/glycerol mixture with η_w = 2 mPa·s ($\eta_w << \eta_o$). After tilting the liquid-infused surfaces by an angle α, we measure the constant drop velocity V (reached after a few millimetres of descent) using a video-camera. In this stationary regime, the friction F is known, since it balances the weight $\rho g \Omega \sin\alpha$, where ρ is the water density, Ω the drop volume, and g the gravitational acceleration. Varying the tilting angle α from 1° to 40° increases friction by about two decades, which makes it possible to investigate the relationship between friction and speed thoroughly.

In Fig. 2a, we plot the drop velocity V as a function of $\sin\alpha$, the slope of the liquid-infused material having small pillars (h = 2 µm). As reported in the literature [6], the graph evidences a scaling behaviour and we deduce from the slope 3/2 drawn across the data that velocity increases as the power 2/3 of the driving force, confirming the non-linear character of the mobility on LIS. A second series of experiments is performed on much taller pillars (h = 75 µm and h = 130 µm), a situation less explored despite its practical interests – the reservoir of oil inside the pillars being then about 50 times larger than previously. As observed in Fig. 2b, a scaling law is also observed, the dashes showing a slope similar to that in Fig. 2a. This result appears robust, being valid for two pillar heights and for a variation of the drop velocity by two orders of magnitude. But it is also surprising since switching from short to large pillars should manifest in the absence or presence of Landau-Levich films, respectively, making the hydrodynamics of the films and thus friction different in both cases.

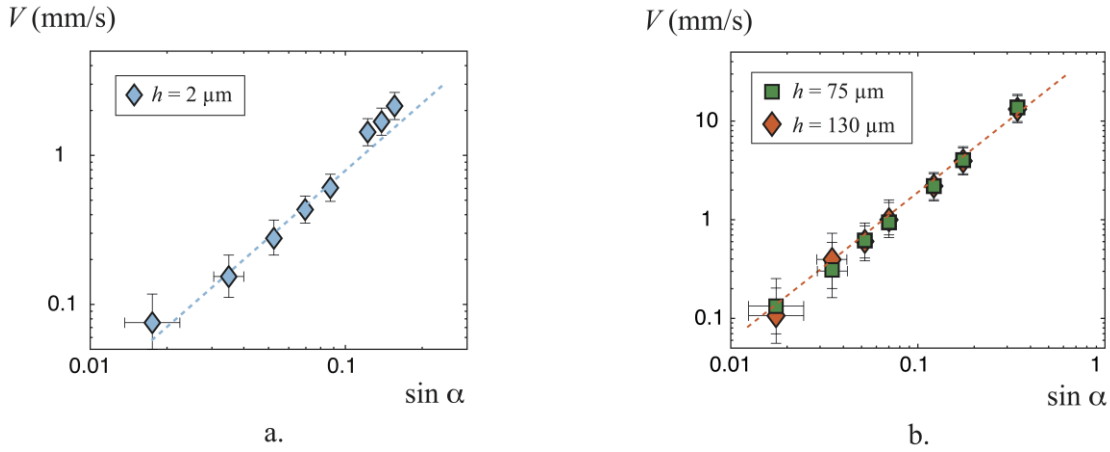

FIG. 2: Speed V of water-glycerol drop (η_w = 2 mPa·s, Ω = 20 µL) running down an impregnated, textured material (η_o = 100 mPa·s), tilted by an angle α, as a function of the slope sinα. We compare what happens on short pillars (**a,** h = 2 µm) and tall pillars (**b,** h = 75 µm and h = 130 µm), two situations for which the physics is quite different: Landau-Levich films are expected on short pillars while they get absorbed in the tall texture. However, scaling laws with the same exponent (3/2, shown by dashes) are observed in both cases.

We now discuss a possible origin for the universal scaling observed for the drop mobility on LIS and further explore differences between the two experiments reported in Fig. 2.

The complex nature of interfaces on a LIS

As sketched in Fig. 1a, the existence of four phases (solid, oil, water and air) in the wetting of LIS generates multiple kinds of interfaces close to which dissipation can take place. We wonder whether all these regions equally contribute to the total friction F and how the texture topology affects friction. In the following, we use the notation F_i to refer to the friction in region i. As pointed out by Daniel *et al.* [7] and by Keiser *et al.* [6], oil feet should be dynamically reshaped, which generates original sources of friction compared to more usual cases.

(1) Oil films may form at the rear of feet (regions 2 and 4 in Fig. 1a). In the Landau-Levich (LL) framework [11], a foot is deformed by a distance $l \sim RCa^{1/3}$, leading to a film thickness $\varepsilon \sim RCa^{2/3}$, where R is the drop radius and Ca is the capillary number at deposition ($Ca = \eta_o V/\gamma_{ow}$ in region 2, $Ca = \eta_o V/\gamma_o$ in region 4, with γ_{ow} and γ_o the oil-water and oil-air tensions, respectively). This classical result can be markedly corrected on pillars, depending on the ratio between the thickness ε and the pillar height h: as shown by Seiwert *et al.* [12], a LL film is expected only for $h < \varepsilon$, while slippage induced in the opposite limit ($h > \varepsilon$) prevents oil deposition above tall pillars. This criterion can be expressed in term of velocity: LL films exist if the drop velocity V is larger than $V^* \sim (\gamma/\eta_o)(h/R)^{3/2}$. On short pillars, this criterion is always satisfied, while it can never be met on tall ones, V^* increasing by a factor 1000 when multiplying h by 100. Using interferometric measurements, Daniel *et al.* directly

observed this wetting transition for drops on LIS, with a prefactor of order 3 for a pillar density ϕ = 25% [7]. It should be noted though that this prefactor decreases as the pillar density increases, as recently observed for droplets confined in Hele-Shaw cells [14]. Coming back to the experiments in Fig. 2 (with ϕ = 25%), V^* is 13 mm/s for $h \approx$ 100 µm, a speed comparable to the maximal speed reached in our experiments. Hence, we do not expect LL films on such tall pillars. Conversely, V^* falls to 40 µm/s for $h \approx$ 2 µm, so that LL deposition should concern the whole range of explored velocities for short pillars. In the latter case, the corresponding friction F_2 and F_4 scales as $2\pi(\eta_o V/\varepsilon)lR$, that is, $F_2 \sim 2\pi\gamma_{ow}RCa^{2/3}$ in region 2 and $F_4 \sim 2\pi\gamma_o RCa^{2/3}$ in region 4. These two quantities of similar amplitude are not linear in velocity, a consequence of the difference in speed dependency of l and ε. Conversely, LL-friction can be simply neglected on tall pillars (or below V^*), which does not explain the scaling observed in that case.

(2) Yet, Keiser *et al.* reported that friction depends on the pillar density ϕ [6], which does not appear in (1). Oil feet move on a mixture of solid and oil (regions 1 and 3 in Fig. 1a), which generates a dynamic angle θ at the front [15-20]. At small θ, the viscous force there can be written $\int(\eta_o V/\theta x)R\mathrm{d}x$, where θx is the wedge thickness at a distance x from its tip. Introducing the meniscus size a (typically 50 µm) and a molecular size b as cut-off distances, we deduce a friction $F_{1/3} \sim (\eta_o V/\theta)R\ln(a/b)$ [18-19]. The logarithmic factor, typically ~10, reflects the enhancement of the viscous force at contact lines. The model must be corrected on infused materials: the foot can slip on the thick oil layer between pillars, so that dissipation mainly takes place on the pillar tops. Restricting friction to these tops provides: $F_{1/3} \sim (\eta_o V/\theta)\phi R\ln(a/b)$. Balancing $F_{1/3}$ with the capillary force $\gamma R(1-\cos\theta) \approx \gamma R\theta^2/2$ yields Tanner's law, $\theta \sim Ca^{1/3}$ [15] and an explicit formula for the friction, $F_{1/3} \sim \phi^{2/3}\ln^{2/3}(a/b)\,\gamma RCa^{2/3}$, with $\gamma = \gamma_o$ in region 1 and $\gamma = \gamma_{ow}$ in region 3. This friction being independent of the pillar's height, it is relevant on any kind of LIS – in particular on tall pillars, where there is no film deposition: this may explain the non-linear character of the scaling observed in Fig. 2a. It should also be noted that the presence of LL-films on small pillars (or for $V > V^*$) may significantly reduce this friction in region 3.

Still, other dissipation mechanisms can be discussed. For instance, the friction in the subjacent film (region 5 in Fig. 1a) turns out to be negligible, owing to the modest value of the velocity V_i at the oil/water interface. The stress balance at this interface writes $\eta_w V/R \sim \eta_o V_i/h$, which yields: $V_i \sim V\,\eta_w h/\eta_o R$. The corresponding force is $(\eta_o V_i/h)\,R^2 \sim \eta_w VR$, indeed much smaller than other viscous frictions for $\eta_w << \eta_o$. Smith *et al.* [4] finally considered the friction in the bulk of the foot (with size a), obtained by integrating the viscous stress $\eta_o V/a$ over the surface area $2\pi aR$ [4]. The corresponding friction $F \sim 2\pi\eta_o VR \sim 2\pi R\gamma Ca$ is linear in velocity, and thus expected to be negligible compared to the line friction in $Ca^{2/3}$ at small Ca.

Back to experiments

We showed that dissipation at the foot fronts (regions 1 and 3) always needs to be considered, while friction in rear sides (regions 2 and 4) can be switched on and off by varying pillar height h or drop velocity V. Despite different physical contents, both frictions at the front and rear sides of the foot scale as $\gamma RCa^{2/3}$, which explains why the total friction F most generally scales as the power 2/3 of V (Fig. 2). We can test the model more accurately by comparing our data to expected behaviours, as done in Figs. 3a and 3b where we also include data obtained by Daniel *et al.* with similar texture.

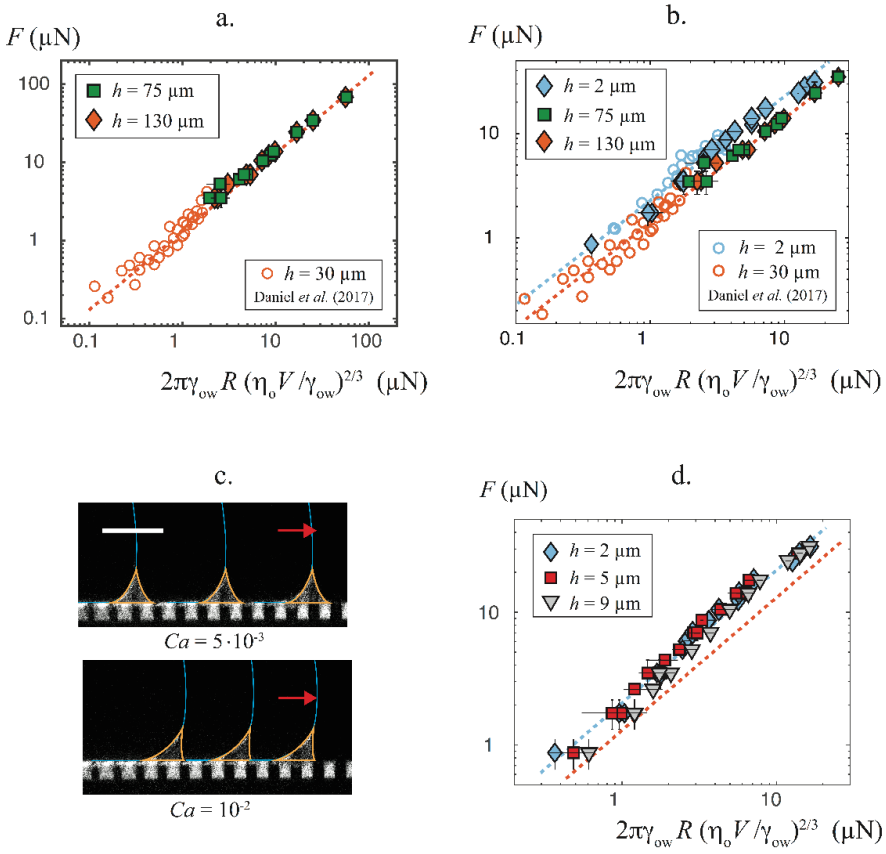

FIG. 3: Friction of drops ($\eta_w = 2$ mPa·s) running down tilted LIS ($\eta_o = 100$ mPa·s). **a.** Friction F as a function of the scaling when dissipation is localised in the front foot, as expected for tall pillars (h = 75 μm, green squares; h = 130 μm, orange diamonds; h = 30 μm, orange circles, data by Daniel *et al.* [7]). Dashes show a slope 1. **b.** Comparison between the friction on short (h = 2 μm, blue diamonds, our data, and empty circles, data from Daniel *et al.* [7]) and tall pillars (h = 75 μm, green squares; h = 130 μm, orange diamonds). Orange and blue lines have a slope 1 with respective prefactors of 1.4 and 2.3 that stress the augmented friction on short pillars. **c.** Chronophotographs of the front foot of a moving drop. Laser scanning confocal microscopy and fluorescent dye allow us to distinguish the oil (in grey) from the rest (water, solid and air), in black. Images are respectively separated by 11.7 s (first picture, drop velocity $V = 10$ μm/s) and 1.7 s (second picture, $V = 200$ μm/s). The contour of the drop is highlighted in blue, and that of the meniscus in orange. The scale bar is 100 μm. **d.** For pillars with intermediate size (h = 5 μm and 9 μm), we observe a transition between the two regimes of friction (drawn with the orange and blue lines), a consequence of the Landau-Levich transition at sufficiently large capillary number.

These graphs allow us not only to test the scaling but also to compare friction on short and tall pillars. All data nicely collapse on a line of slope 1 (dashes) but the numerical coefficient depends on the category of pillars: friction is increased by about 60% on short pillars, compared to that on tall ones. These facts agree with our model. We indeed expect an additional LL friction on short pillars; and the coefficient of the front friction, $[\phi \ln(a/b)]^{2/3}$ (that reflects both the composite nature of the substrate and the amplification of viscous effects in a wedge), should be of order unity, that is, comparable to the coefficient in the rear friction. We can finally complete these findings by two supplementary experiments.

(1) Since dissipation in the foot front was assumed to be always at stake, it is essential to show the reality of dynamic angles in regions 1 and 3. To that end, we visualize the moving menisci using laser scanning confocal microscopy, as described in appendix. A water drop ($\Omega \approx 20\,\mu L$) placed on a liquid-infused surface (h = 20 µm) is moved with a needle, parallel to the substrate, in the range of capillary numbers explored in Fig. 3a. Fig. 3c shows three successive images of region 1 at $Ca = 5.10^{-3}$ and $Ca = 10^{-2}$. Incorporating a fluorescent dye in the oil makes it grey in the image and visible both in the texture and in the foot, while water, pillars, and air appear in black [21]. Two major observations can be made. Firstly, the oil meniscus is stationary, even at the larger velocity. This assumption in the model was not obvious since flows might redistribute oil from the front to the rear of the drop, making, for instance, the foot globally smaller when velocity is higher and/or with size a varying along the motion. Secondly, the foot is asymmetric, as we assumed: the rear (region 2) meets tangentially the substrate (and the resolution of the technique even confirms the absence of Landau-Levich deposition on these high pillars), while the flow stiffens the front (region 1) and produces a dynamic contact angle whose value increases with the drop speed. This also shows that viscous dissipation in region 2 (and 4) is not large enough to deform an oil meniscus on tall pillars from its quasi-static configuration, which justifies that we do not consider this dissipation in our balance.

(2) We can also consider pillars with intermediate height. Contrasting with the previous asymptotic situations, we then expect a transition to Landau-Levich deposition within the range of explored speed ($V^* \approx 300$ µm/s for h = 9 µm), which should impact the friction. As seen in Fig. 3d, data for h = 9 µm (grey triangles) leave the regime of "high friction" at large Ca for the regime of "low friction" at small Ca. The drop speed at the transition is $V^* \approx$ 200 µm/s, in reasonable agreement with our expectation. Interestingly, the transition is found to be shifted to smaller Ca for shorter pillars (h = 5 µm, red squares) – in agreement with the fact that LL-films appear at a lower velocity on smaller texture. Hence varying the texture height allows us to control the resistance (and thus the speed) of drops on infused materials. This action is efficient since shortening the pillars roughly doubles the friction, without modifying its non-linear character in velocity.

Drops confined in a Hele-Shaw cell

In order to test the universality of the scaling laws, we now observe drops moving in an Hele-Shaw cell (with gap H = 1110 µm) whose both plates are textured and impregnated. Drops adopt a pancake shape [22-24], as sketched in Fig. 3a. Increasing the tilt angle of the cell, we can vary the drop velocity from 0.01 mm/s to 20 mm/s, allowing us to measure the relationship between friction and velocity by more than three decades in speed.

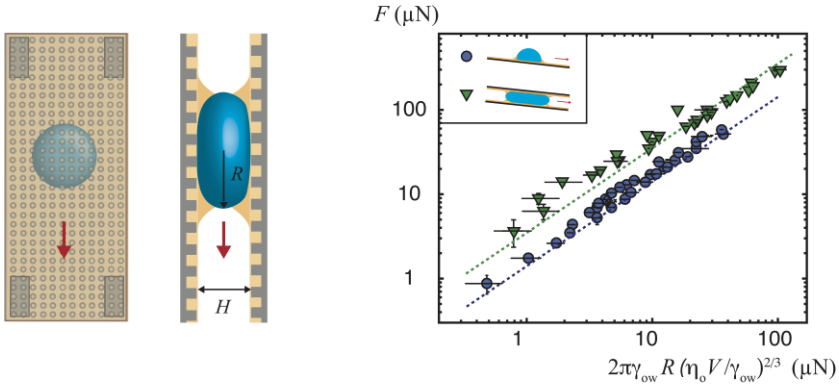

FIG. 4: a. Front and side views of a Hele-Shaw LIS. A drop with radius R is confined between two LIS impregnated with silicon oil and separated by a distance $H < R$. The cell is tilted by an angle α (α = 90° in the schematics). **b.** Friction F of drops as a function of the scaling form $2\pi\gamma_{ow}R\,(\eta_o V/\gamma_{ow})^{2/3}$ on LIS (blue circles) and in Hele-Shaw LIS (H = 1110 µm, green triangles). All surfaces have the same texture (square lattice of circular pillars, h = 20 µm, ϕ = 23%). Oil and water viscosities are respectively η_o = 100 mPa·s and η_w = 2 mPa·s. Drop volumes are varied between 10 and 30 µL and tilt angles between 1° and 90°. Lines have a slope 1 and numerical factors of 1.4 (blue line), as in Fig. 3, and 3.5 (green line). The small deviation at small speed (tilting angle < 5°) may be attributed to some residual adhesion, enhanced in this configuration.

Our results are displayed in Fig. 4b. When plotting the friction as a function of the scaling form $2\pi\gamma_{ow}R(\eta_o V/\gamma_{ow})^{2/3}$, we observe that data align along two well-separated lines of slope 1. The numerical coefficient provided by the fit is 3.5 (green dashes) in the Hele-Shaw cell, that is, about twice larger than on a LIS (blue dashes, where the numerical factor is 1.4). Even if the Hele-Shaw configuration strongly modifies the drop geometry, the foot dissipation should indeed simply double in a cell, that is, when doubling the number of feet.

Bubbles on LIS

We finally consider a gas bubble running up a tilted liquid-infused surface immersed in water (Fig. 5a). Then, water and air are inverted, compared to the previous configurations. This is reminiscent of the historical experiment of Bretherthon [25], where a bubble confined in a capillary tube of radius R is driven by pressure. Then, the friction in the liquid wedge at the

front of the drop was shown to scale as $\gamma RCa^{2/3}$. Non-confined bubbles moving on smooth immersed solids have also been discussed (Aussillous & Quéré [26], Cantat [27], Le Merrer *et al.* [28]), a case where the deposition of a film between the bubble and the solid substrate generates a wedge friction still scaling as $Ca^{2/3}$. The situation of bubbles moving on immersed LIS might induce differences: the presence of oil menisci generates two extra dissipative terms, in regions 1 and 4; in addition, the solid surface is not smooth but textured.

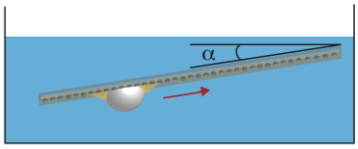

a.

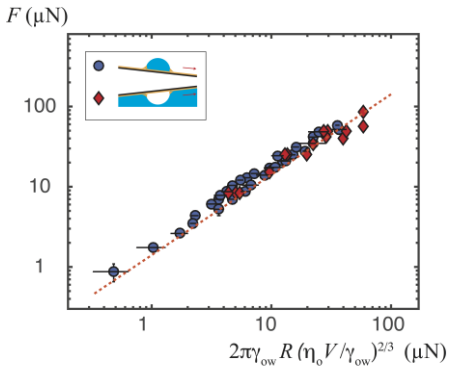

b.

FIG. 5: a. Air bubble with volume Ω rising on a tilted LIS immersed in water. Water and air are inverted, compared to Fig. 1a. **b.** Friction F of drops or bubbles as a function of the scaling form $2\pi\gamma_{ow}R\,(\eta_o V/\gamma_{ow})^{2/3}$ for drops (blue circles) or bubbles (red diamonds) on a LIS with h = 20 μm and ϕ = 23%. Water viscosity is η_w = 2 mPa·s, and oil viscosity is η_o = 100 mPa·s for the drop and η_o = 10, 100 or 1000 mPa·s for the bubble. Drop and bubble volumes are 20 μL and 10 μL, respectively, and tilt angle is varied between 1° and 30°. The line has a slope 1 and a numerical factor of 1.4, as in Fig. 3.

Yet, data for drops and bubbles are found to be superimposed (Fig. 5b), contrasting with what we would find if we did the same inversion on a regular, hydrophobic solid. This confirms the negligible role of water and air viscosity in the viscous dissipation, and eventually provides an independent proof of the role of the oil meniscus (equally present for drops and bubbles) in the dissipation associated with the fluid motion.

Summary

On the whole, the friction force on a LIS most generally scales as $V^{2/3}$, a unique behaviour despite the multiple possible causes of dissipation – that eventually condense in a universal friction law. In addition, the numerical coefficient in the friction (and thus the drop speed) can

be efficiently tuned by the pillar height, which shows that the use of texture is not only relevant for diminishing the liquid adhesion, but also to adjust its friction.

Acknowledgements

This work has received the support of Institut Pierre-Gilles de Gennes (équipement d'excellence Investissements d'avenir, programme ANR-10-EQPX-34), and the European Union's Horizon 2020 research and innovation program ITN LubISS No 722497. The authors thank A. Kaltbeitzel and A. Naga for taking the confocal images and for stimulating discussions.

Appendix 1:
Fabrication of the surfaces and imaging

Textured surfaces are obtained using SU-8 photolithography. A layer of SU-8 resin is spin-coated on the surface of a clean, dehydrated silicon wafer. The rotating speed imposes the deposited thickness and thus the pillar height. Reticulation of pillars is performed by UV-light through a mask and the obtained texture consists of square arrays of either circular or rectangular pillars. The second scale of roughness is added by dipping the microtextured material in a solution of Glaco Mirror Coat (Soft 99). After evaporation of the solvent (drying at 70°C for 30 min.), both the substrate and the pillars are coated with a layer of hydrophobic nanobeads (typical size 30 nm), as shown in Fig. S1.

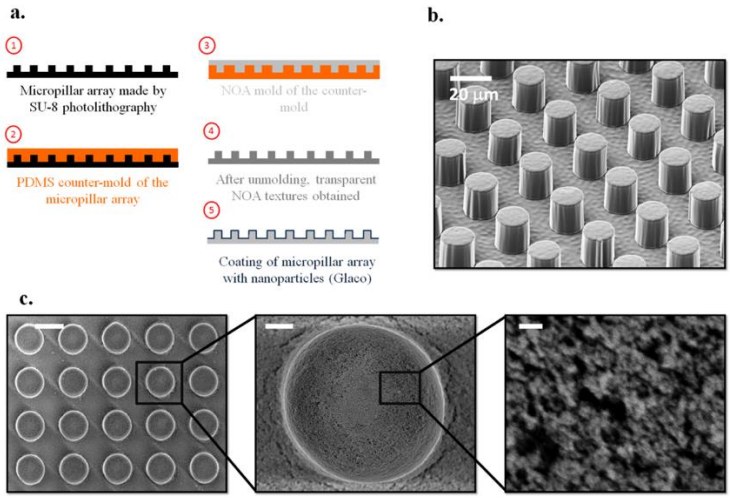

FIG. S1: a. Schematic of the main steps to obtain transparent textured surfaces in NOA optical adhesive on a glass slide. **b.** SEM images of the textures made of NOA optical adhesive on a glass slide (courtesy of Florian Geyer, MPIP). **c.** Close-up on the nano-roughness at the pillar tops on the Glaco treated surfaces. Left: top view of the pillar network (bar: 40 µm). Middle: close-up on one pillar (bar: 4 µm). Right: close-up on the pillar top (bar: 400 nm).

The procedure is repeated three times to ensure a homogeneous coating. Impregnation of the surfaces is then achieved by capillarity, taking special care not to over-impregnate the surfaces. To that end, surfaces are tilted with their lower side in contact with a bath of silicone oil of viscosity η_o so that oil rises within the texture. Transparent surfaces (necessary for the experiments in the Hele-Shaw cell) are obtained by two additional steps: 1) fabrication of a PDMS counter-mold of the SU-8 texture; 2) mold of this counter-mold with a transparent optical adhesive (NOA, Norland Optical Adhesive) on a glass slide. This protocol is shown in Fig. S1a, and SEM images of the transparent surfaces obtained (60 mm x 24 mm, thickness: ≈ 170 μm) with the NOA optical adhesive before and after the coating with nanobeads are shown in Figs. S1b and S1c, respectively.

Silicone oil does not completely wet neither SU-8 nor NOA in an aqueous environment. Thus, direct contact between the drop and the pillar tops exists if no Glaco treatment is made [6], which explains why the two scales of roughness are necessary to provide an ultra-low adhesion of water with roll-off angles below 1° for a 20 μL drop [6, 13]. The impregnation method must also be stressed. Beyond introducing a layer of oil of uncontrolled thickness, over-impregnation will profoundly affect the dissipation of the front menisci (through the logarithm factor discussed in the main paper). As this thickness is not controllable over an extended period of time, over-impregnation will lead to scattered measurements of the friction force.

An inverted laser scanning confocal microscope (Leica TCS SP8 SMD) equipped with a 40x/1.11 water immersion objective lens (Olympus) was employed to image the oil meniscus surrounding the aqueous drop. The free working distance of the objective is 0.65 mm. The drop is moved by a glass capillary that pins the liquid and entrains it. Scanned areas are 400 x 400 μm^2, if not stated otherwise. Horizontal and vertical resolutions are ~500 nm and ~1 μm, respectively, and the time span between successive images is 0.78 s (1.29 fps). The scanning frequency is 400 Hz. Images are acquired at different heights with respect to the bottom surface of the micropillar substrate. The silicone oil is dyed with a TDI-derivative (terrylene diimide-based dye, [29], or NileRed from Sigma Aldrich). After impregnation, the fluorescence of the silicone oil within the texture and in the meniscus appears in grey, while pillars, water and air remain black. All chemicals were used as received. Processing of the confocal images is done the Java-based open-source image processing software ImageJ. Contrast and brightness are optimized, and smoothening algorithms are applied to further improve the image quality by minimizing the amount of intensity variations.

Appendix 2:
Complements in Hele-Shaw cells

Due to the confined geometry, the experiments in the Hele-Shaw cell show scaling laws that slightly differ from the one derived in Keiser *et al.* [6]. We present here supplementary results about this special geometry (Figure S2).

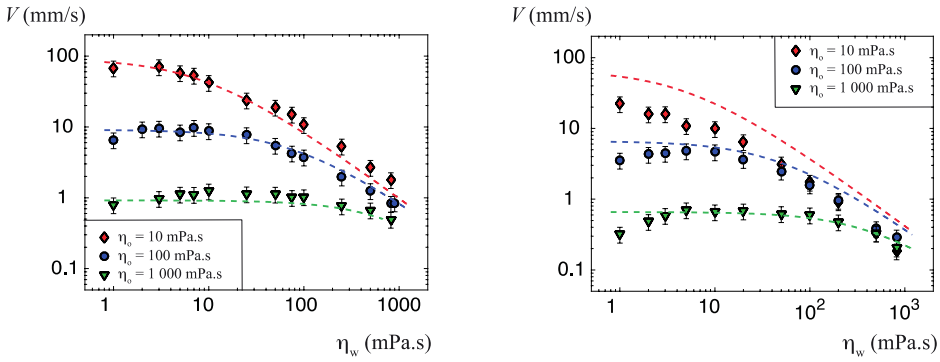

FIG. S2: Speed V of water/glycerol mixtures (Ω = 10 µL, viscosity η_w) confined in a vertical Hele-Shaw cell of thickness 1110 µm (**a**) or 720 µm (**b**). The cell walls are LIS impregnated by silicone oil with viscosity η_o = 10 mPa·s (red diamonds), 100 mPa·s (blue circles) or 1000 mPa·s (green triangles). At low η_w, the speed is nearly independent of η_w. At large η_w, the speed becomes inversely proportional to η_w. Dashes show the speed obtained by balancing gravity with the total friction in the drop and in the menisci (see text). For the Hele-Shaw cell of thickness 720 µm, the agreement between experiments and model is less convincing at low oil viscosity. The drops then become slightly elliptic, that is, of larger perimeter, which might contribute to increase the viscous dissipation and thus lower the velocity.

First, the viscosity of the drop has been varied to explore regions not only with $\eta_o >> \eta_w$ but also with $\eta_o << \eta_w$. Two main regimes appear (Fig. S2), showing that dissipation is either localized in the oil (when $\eta_o >> \eta_w$) or in the drop (when $\eta_o << \eta_w$), as known for non-confined drops [6, 8]. At high drop viscosity ($\eta_w >> \eta_o$), dissipation takes place in the drop and the friction is proportional to the speed (Fig. S3a).

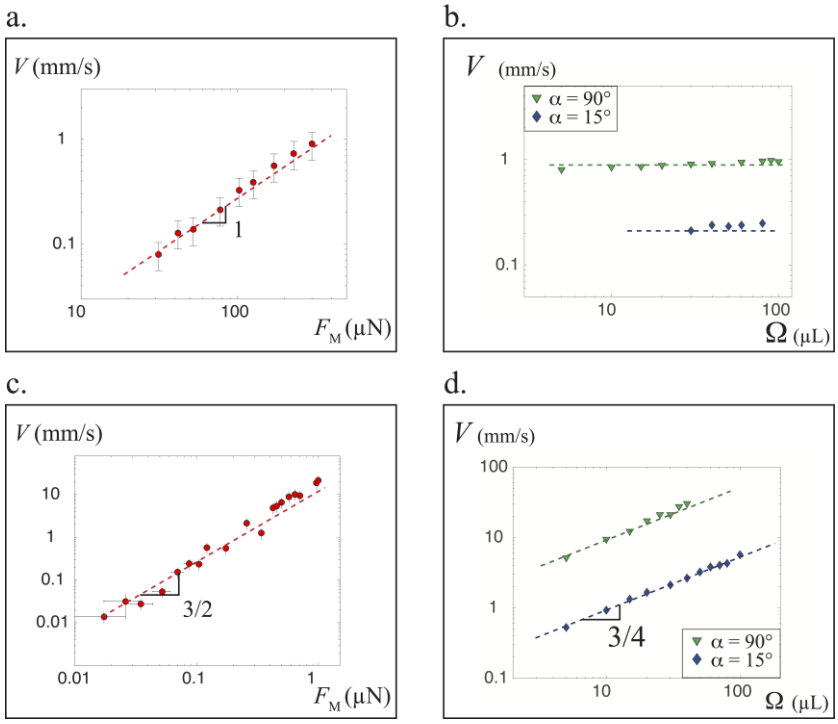

FIG. S3: a. Speed V of a drop (Ω = 30 µL, η_w = 900 mPa·s) in a Hele-Shaw cell impregnated with silicone oil with viscosity η_o = 100 mPa·s as a function of the driving force $F_M = \rho g \Omega \sin\alpha$. For $\eta_w >> \eta_o$, dissipation localizes in the drop, which makes the friction linear in speed. **b.** Then, the speed is observed to be independent of the drop volume Ω, as predicted by our model. **c.** Same experiment as in a for η_w = 2 mPa·s and η_o = 100 mPa·s ($\eta_w << \eta_o$). Then dissipation localizes in the oil and the dependency between friction with speed becomes non-linear. **d.** In this case, the speed varies as the power ¾ of Ω again in accord with our expectations.

In this simplified configuration (compared to the case of a non-confined drop, explore by Keiser *et al*. [6]), we can exactly express the prefactor in the Poiseuille force, which yields: $F_\eta = 12\pi R^2 \eta_w V/H$. Balancing this friction with the driving force $\rho g \pi R^2 H \sin\alpha$, we get:

$$V = \rho g H \sin\alpha / 12\eta_w$$

Due to the pancake shape of the drop in this geometry, the velocity is found to be independent of the drop radius (and volume), which is indeed observed in Fig. S3c.

In the opposite limit ($\eta_o >> \eta_w$), the dissipation localizes in the oil foot, as described in the main text, leading to a non-linear relation between the friction force and speed (Fig. S3c). Balancing the driving force $\rho g \pi R^2 H \sin\alpha$ with the friction force $F_\eta = 2\pi R \phi \gamma Ca^{2/3} L$ leads to a new expression for the drop speed:

$$V = (\rho g \sin\alpha / 2\phi L)^{3/2} (\Omega H/\pi)^{3/4} / \eta\gamma^{1/2}$$

Both the scaling of the speed V with the driving force and with the volume are verified in the Figs. 3c and 3d, where the dashes show the slopes 3/2 and 3/4, respectively.

A general relationship between drop velocity and viscosity can finally be obtained by solving the implicit equation $\rho g \Omega \sin\alpha = 2(2\pi R \gamma Ca^{2/3} \phi^{2/3} \ln^{2/3}(a/b)) + 12\pi R^2 \eta_w V/H$, the balance of gravity with the total friction (in both oil menisci and in the drop). Doing so, we find a very good agreement (without any adjustable parameters other than the logarithm factor taken as 10, its expected value) between the model and the whole set of data, as seen in Fig. S2.

References

1. Quéré, D. Non-sticking drops. *Rep. Prog. Phys.* 68, 2495–2533 (2005).
2. Wong T.S., Kang S.H., Tang S.K., Smythe E.J., Hatton B.D., Grinthal A. and Aizenberg J. Bioinspired self-repairing slippery surfaces with pressure-stable omniphobicity. *Nature* 477, 443–447 (2011).
3. Lafuma A. and Quéré D. Slippery pre-suffused surfaces. *EPL* 96, 56001 (2011).
4. Smith J.D., Dhiman R., Anand S., Reza-Garduno E., Cohen R.E., McKinley G.H. and Varanasi K.K. Droplet mobility on Lubricant-Impregnated Surfaces. *Soft Matter* 9, 1772–1780 (2013).
5. Solomon B.R., Khalil K.S., and Varanasi K.K. Drag reduction using lubricant-impregnated surfaces in viscous laminar flow. *Langmuir* 30, 10970–10976 (2014).

6. Keiser A., Keiser L., Clanet C. and Quéré D. Drop friction on liquid-infused materials. *Soft Matter* 13, 6981–6987 (2017).
7. Daniel D., Timonen J.V.I., Li R., Velling S.J. and Aizenberg J. Oleoplaning droplets on lubricated surfaces. *Nat. Phys.* 13, 1020–1025 (2017).
8. Daniel D., Timonen J.V.I., Li R., Velling S.J., Kreder M. J., Tetreault A. and Aizenberg, J. Origins of extreme liquid repellency on structured, flat, and lubricated surfaces. *Phys. Rev. Lett.* 120, 244503 (2018).
9. Sadullah M.S., Semprebon C. and Kusumaatmaja H. Drop dynamics on Liquid Infused Surfaces: The role of the wetting ridge. *Langmuir*, 34, 8112–8118 (2018).
10. Asmolov E.S., Nizkaya T.V., and Vinogradova O.I. Enhanced slip properties of lubricant-infused grooves. *Phys. Rev. E* 98, 033103 (2018).
11. Landau L. and Levich B. Dragging of a liquid by a moving plate. *Acta Physicochim. USSR* 17, 42–54 (1942).
12. Seiwert J., Clanet C. and Quéré D. Coating of a textured solid. *J. Fluid Mech.* 669, 55–63 (2011).
13. Guan J.H., Ruiz-Gutiérrez E., Xu B.B., Wood D., McHale G., Ledesma-Aguilar R. and Wells G.G. Drop transport and positioning on lubricant-impregnated surfaces. *Soft Matter* 13, 3404–3410 (2017).
14. Keiser L., Keiser A., L'Estimé M., Bico J. and Reyssat E., Motion of viscous droplets in rough confinement: paradoxical lubrication, *Phys. Rev. Lett.* 122, 074501 (2019).
15. Tanner L. The spreading of silicone oil drops on horizontal surface, *J. Phys. D* 12, 1473–1484 (1979).
16. Cox R.G. The dynamics of the spreading of liquids on a solid surface. Part 1. Viscous flow. *J. Fluid Mech.* 168, 169–194 (1986).
17. Voinov O.V. Hydrodynamics of wetting. *Fluid Dyn.* 11, 714–721 (1976).
18. De Gennes P.G. Wetting: statics and dynamics. *Rev. Mod. Phys.* 57, 827–863 (1985)
19. Bonn D., Eggers J., Indekeu J., Meunier J. and Rolley E. Wetting and spreading. *Rev. Mod. Phys.* 81, 739–805 (2009).
20. Snoeijer J.H. and Andreotti B. Moving contact lines: scales, regimes, and dynamical transitions. *Annu. Rev. Fluid Mech.* 45, 269–292 (2013).
21. Schellenberger F., Xie J., Encinas N., Hardy A., Klapper M., Papadopoulos P., Butt H.J. and Vollmer D. Direct observation of drops on slippery lubricant-infused surfaces. *Soft Matter* 11, 7617–7626 (2015).
22. Huerre A., Theodoly O., Leshansky A.M., Valignat M.P., Cantat I. and Jullien M.C. Droplets in microchannels: dynamical properties of the lubrication film. *Phys. Rev. Lett.* 115, 064501 (2015).
23. Yahashi M., Kimoto N. and Okumura K. Scaling crossover in thin-film drag dynamics of fluid drops in the Hele-Shaw cell. *Sci. Rep.* 6, 31395 (2016).
24. Keiser L., Jaafar K., Bico J. and Reyssat E. Dynamics of non-wetting drops confined in a Hele-Shaw cell. *J. Fluid Mech.* 845, 245–262 (2018).
25. Bretherton F.P. The motion of long bubbles in tubes, *J. Fluid Mech.* 10, 166–188 (1961).
26. Aussillous P. and Quéré D. Bubbles creeping in a viscous liquid along a slightly inclined plane. *Europhys. Lett.* 59, 370-376 (2002).
27. Cantat I. Liquid meniscus friction on a wet plate: Bubbles, lamellae, and foams. *Physics of Fluids* 25, 031303 (2013).
28. Le Merrer M., Lespiat R., Höhler R. and Cohen-Addad S., Linear and non-linear wall friction of wet foams. *Soft Matter* 11, 368–381 (2015).
29. Jung C., Müller B.K., Lamb D.C., Nolde F., Müllen K. and Bräuchle C. A new photostable terrylene diimide dye for applications in single molecule studies and membrane labeling. *J. Am. Chem. Soc.* 128, 5283–5291 (2006).